An improved energy method for determining Young's modulus by instrumented indentation using a Berkovich tip

Dejun Ma
Department of Mechanical Engineering, The Academy of Armored Forces Engineering, Beijing 100072, People's Republic of China

Chung Wo Ong[a)]
Department of Applied Physics and Materials Research Center, The Hong Kong Polytechnic University, Hung Hom, Kowloon, Hong Kong, People's Republic of China

Taihua Zhang
State Key Laboratory of Nonlinear Mechanics (LNM), Institute of Mechanics, Chinese Academy of Sciences, Beijing 100080, People's Republic of China

(Received 20 September 2007; accepted 14 March 2008)

We previously proposed a method for estimating Young's modulus from instrumented nanoindentation data based on a model assuming that the indenter had a spherical-capped Berkovich geometry to take account of the bluntness effect. The method is now further improved by releasing the constraint on the tip shape, allowing it to have a much broader arbitrariness to range from a conical-tipped shape to a flat-ended shape, whereas the spherical-capped shape is just a special case in between. This method requires two parameters to specify a tip geometry, namely, a volume bluntness ratio V_r and a height bluntness ratio h_r. A set of functional relationships correlating nominal hardness/reduced elastic modulus ratio (H_n/E_r) and elastic work/total work ratio (W_e/W) were established based on dimensional analysis and finite element simulations, with each relationship specified by a set of V_r and h_r. Young's modulus of an indented material can be estimated from these relationships. The method was shown to be valid when applied to S45C carbon steel and 6061 aluminum alloy.

I. INTRODUCTION

Young's modulus is one of the most important mechanical properties of a material. Instrumented indentation is distinctive among all techniques for measuring Young's modulus, because it is particularly suitable for small-scaled specimens.[1–8] Conventionally, a result is derived from indentation data according to Oliver and Pharr's formulation[4–6]:

$$E_r = \frac{\sqrt{\pi}}{2\beta}\frac{S_u}{\sqrt{A(h_{cm})}} \quad . \tag{1}$$

S_u is the initial slope of an unloading curve. E_r is the reduced modulus, related to the Young's modulus and Poisson's ratio of the indented material (E and ν) and those of the indenter (E_i and ν_i) by the equation $1/E_r = (1-\nu^2)/E + (1-\nu_i^2)/E_i$. β is a constant depending on the shape of the indenter. $A(h_{cm})$ is the projected contact area evaluated at the maximum contact depth h_{cm} corresponding to the maximum indentation depth h_m and maximum load P_m. According to Oliver and Pharr's model, $A(h_{cm})$ can be estimated from the unloading curve, but the result may not be accurate enough, particularly when piling up occurs.

An alternative way to analyze instrumented indentation data is to refer to the energy quantities involved in the process.[9–11] By applying scaling relationships in combination with finite element simulations, Cheng et al.[12–14] verified the existence of a functional relationship:

$$H/E_r = g(W_e/W) \quad , \tag{2}$$

where $H \equiv P_m/A(h_{cm})$ is the hardness. W_e and W are the elastic work and total work, which are equal to the areas under the unloading and loading curves, respectively. By combining Eqs. (1) and (2) to eliminate $A(h_{cm})$, E_r can be determined as:

$$E_r = [\pi/(2\beta)^2]\, g(W_e/W)[S_u^2/P_m] \quad . \tag{3}$$

[a)]Address all correspondence to this author.
e-mail: apacwong@inet.polyu.edu.hk
DOI: 10.1557/JMR.2008.0257

This method is different from Oliver and Pharr's method, because it has no need to determine h_{cm} [or $A(h_{cm})$] by some indirect means as is the case in Oliver and Pharr's model, such that no error would be generated from this process. However, the method was developed only for an ideally sharp conical indenter, so the influence of the bluntness of the indenter is not included. Moreover, the determination of S_u may have some uncertainty due to, for example, vibration noise, the influence of which is serious for a shallow indentation. This error is magnified after taking the square of S_u, which eventually propagates to the estimated value E_r through Eq. (3).

Recently, we proposed a new method to analyze indentation data for estimating the elastic modulus of a material, which not only can prevent indirect estimation of h_{cm}, but can also take the bluntness effect into account.[15,16] In this method, a nominal hardness $H_n = P_m/A(h_m)$ is introduced, which is defined as the maximum load P_m divided by the cross-sectional area $A(h_m)$ evaluated at the maximum indentation depth h_m and is therefore different from the conventional hardness H determined with the area evaluated at the maximum contact depth h_{cm}. The bluntness of a nonideally sharp indenter was considered by introducing a parameter named the volume bluntness ratio $V_r \equiv V_{ideal}/V_{blunt}$, where V_{ideal} is the part of volume bounded by the area $A(h_m)$ for an ideally sharp Berkovich indenter (Fig. 1), and V_{blunt} is that for a real indenter. Functional relationships correlating H_n/E_r and W_e/W for various values of V_r were established from the results of finite element analysis (FEA). The Young's modulus of an indented material can thus be estimated according to the experimental values of H_n, W_e, W, and V_r. Because this method is built up based on a spherical-capped indenter model, it can only provide good results when the real indenter tip has a shape close to this model.

In this work, we further modified the aforementioned method by making it suitable to a broad range of tip shapes with more arbitrary bluntness—including the extremely blunt situation. In addition to V_r used in our previous method, a new parameter named the height bluntness ratio $h_r \equiv h_{ideal}/h_m$ is introduced to describe the tip geometry, where h_{ideal} is the distance from the vertex of an ideally sharp conical shape to the area $A(h_m)$. Compared with our previously proposed method just involving one single parameter V_r, the arbitrariness of the shape and bluntness of a real Berkovich indenter tip would be better expressed by the present model, which requires the use of two parameters.

II. TWO-PARAMETER DESCRIPTION OF NONIDEALLY SHARP INDENTERS

An indenter with Berkovich geometry is commonly used in a nanoindentation test. The real indenter geometry is not ideally sharp, whereas the influence of the bluntness of the tip is remarkable in a nanoscaled indentation. For simplicity, a blunt or nonideal Berkovich indenter is approximated by a nonideal conical geometry with a protruding end. The reasonability was based on the fact that the computational load–displacement response produced by using a real Berkovich tip was found to be virtually identical to that produced by a conical tip with a half-included conical angle $\theta = 70.3°$ having the same area-to-depth ratio as that of the real indenter.[17,18] We start from showing three selected cases in Fig. 2, which are drawn to have the same volume bluntness ratio V_r but different height bluntness ratios h_r. Case 1 refers to a flat-end geometry, which has the largest value of h_r and hence is used to represent the extremely blunt situation. Case 2 refers to a conical-tipped geometry with a half-included conical angle α larger than $\theta = 70.3°$. This geometry is thus regarded to be blunter than the ideal one. Since h_r of this model is the smallest one among those of these three models, this geometry is used to represent another extreme situation. The third case is the spherical-capped geometry, which is an intermediate situation between the aforementioned two. One learns from Fig. 2 that though the three models have the same value of V_r, their h_r parameters are different, indicating that a single parameter V_r alone is not enough to fully describe the tip shape, but only can give a primary

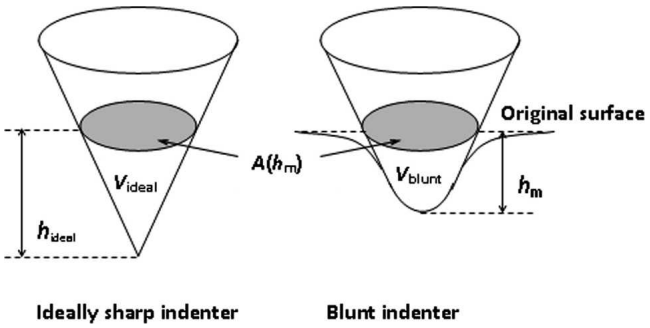

FIG. 1. Schematic diagrams of an ideally sharp indenter and a blunt indenter.

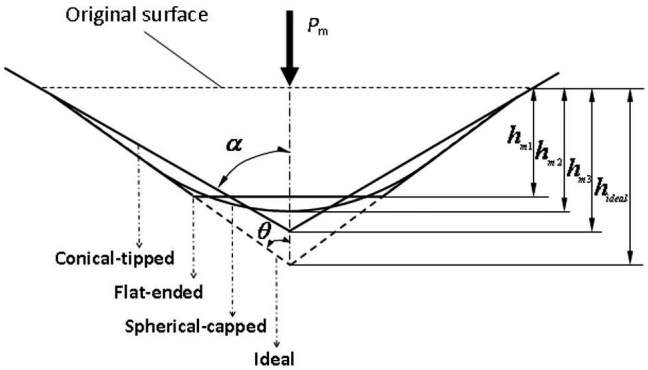

FIG. 2. Three representative blunt geometries and the ideally sharp geometry.

approximation. This motivates the use of two parameters V_r and h_r to describe the real geometry of the tip that in general deviates more or less from the typical ones considering different degrees of bluntness. It is further noted that V_r and h_r are not independent for a specific bluntness type. With the use of suffixes "f," "c," and "s" to label the purely flat-ended case, conical-tipped case, and spherical-capped case, respectively, the first one has $V_r = 1/[1 - (1 - 1/h_{rf})^3]$; the second one has $V_r = h_{rc}$; and the last one has $V_r = 1/[1 - (1 - 1/h_{rs})^3 (1 + \sin\theta)]$ when $V_r \leqslant 1.361$, and $V_r = 2h_{rs}^3/(3h_{rs}^2 + \cot^2\theta)$ when $V_r > 1.361$. The condition $V_r = 1.361$ specifies a situation in which the maximum indentation depth is equal to the distance between the bottom of the spherical cap and the conical-spherical cap interface.

III. NUMERICAL ANALYSIS OF THE NONIDEALLY SHARP INDENTATION

Within the framework of continuum mechanics, we apply the finite element method to investigate the response of the indented material by three representative types of nonideal conical indenters mentioned previously. The indented material is assumed to behave as an isotropic and rate-independent solid and obeys Von Mises yield criterion and pure isotropic hardening rule. The uniaxial stress–strain relations take the form of linear elasticity combined with the Hollomon's power-law hardening, namely:

$$\sigma = \begin{cases} E\,\epsilon, & \epsilon \leqslant \epsilon_y \\ \sigma_y(\epsilon/\epsilon_y)^n, & \epsilon > \epsilon_y \end{cases} \quad , \tag{4}$$

where σ and ϵ are the true stress and true strain, and σ_y and $\epsilon_y = \sigma_y/E$ the yield stress and yield strain. When we assume that the indenter is elastic, and no friction exists between the contact interface and the indenter, the nominal hardness H_n and the work ratio W_e/W are treated as the responses and should be regarded as functions of the elastoplastic properties (E, ν, σ_y, n) of the tested material, the elastic properties (E_i, ν_i) of the indenter, the maximum indentation depth (h_m), and two bluntness ratios (V_r and h_r). The correlations between these quantities are expressed implicitly as:

$$H_n = f_H(E, \nu, \sigma_y, n, E_i, \nu_i, h_m, V_r, h_r) \quad , \tag{5}$$

$$W_e/W = f_W(E, \nu, \nu_y, n, E_i, \nu_i, h_m, V_r, h_r) \quad . \tag{6}$$

According to Dao et al.[17] and Fischer-Cripps,[19] these two functions may be simplified by introducing the quantity E_r to combine the overall elasticity effects of the indenter and the indented material, such that Eqs. (5) and (6) can be expressed as:

$$H_n = f_H(\sigma_y, n, E_r, h_m, V_r, h_r) \quad , \tag{7}$$

$$W_e/W = f_W(\sigma_y, n, E_r, h_m, V_r, h_r) \quad . \tag{8}$$

Applying $\prod$ theorem of dimensional analysis, functions (7) and (8) can be rewritten in the following dimensionless forms:

$$H_n/E_r = \Phi_H(\sigma_y/E_r, n, V_r, h_r) \quad , \tag{9}$$

$$W_e/W = \Phi_W(\sigma_y/E_r, n, V_r, h_r) \quad . \tag{10}$$

Considering that σ_y/E_r in Eq. (10) can be expressed in terms of W_e/W, n, V_r, and h_r, it can be expressed alternatively as:

$$\sigma_y/E_r = \Psi_W(W_e/W, n, V_r, h_r) \quad . \tag{11}$$

By substituting Eq. (11) into Eq. (9) to remove σ_y/E_r, the expression of H_n/E_r becomes:

$$\begin{aligned} H_n/E_r &= \Phi_H[\Psi_W(W_e/W, n), n, V_r, h_r] \\ &= \Gamma_H(W_e/W, n, V_r, h_r) \quad . \end{aligned} \tag{12}$$

To obtain an explicit result, a commercial finite element code ABAQUS[20] having the capability of handling large deformation analysis was employed to simulate the indentation process with nonideal conical indenters. In the calculations, the independent variable σ_y/E_r in Eqs. (9) and (10) was varied in such a way that E_r is kept unchanged by assigning fixed values to E, ν, E_i, and ν_i, and let σ_y vary alone. In particular, E_i and ν_i can be removed to get further simplicity by assuming that the indenter is rigid. As such, E and ν are fixed at 70 GPa and 0.3, while σ_y is assigned to vary in a broad range of 0.0005 to ~10.500 GPa. n is assigned by the values of 0, 0.15, 0.3, and 0.45 in sequence, and V_r by 1, 1.336, 2.547, and 4.764. The settings are kept the same for all cases unless otherwise specified. For each of the three V_r values other than 1, three h_r values corresponding to the three representative types as described in Sec. II are derived. $V_r = 1$ refers to the case of ideal tip shape, where $h_r = 1$. In a finite element simulation, four-node axisymmetric elements are used. The size of the elements was made to have the same size near the contact region, which was sufficiently small to make sure that at least 60 nodes are included in a radial profile across a nominal contact area, which is defined as the cross-sectional area of the indenter evaluated at the maximum indentation depth. The mesh used in our study was designed to be composed of 28,900 quadrilateral elements and 29,241 nodes, and the total degree of freedom (DOF) of the model is 58,140. The overall dimensions of the model in the radial and axial directions are identical, and the radius of the cross-sectional area of the indenter at the maximum indentation depth is constantly below 1/20 of the overall radius of the model. A sensitivity test was performed by looking at the result obtained after refining the mesh size by one-half and doubling the dimensions of the model in both radial and vertical directions. The values of the peak load P_m and the work ratio W_e/W thus obtained do not vary more than 0.5% from those obtained

by using the original model, confirming that the original settings of meshing and overall dimension of the model are suitable for simulating a hypothetical indentation made on a semi-infinite solid.

Figure 3 shows some exemplified normalized load–displacement curves obtained from simulations with the settings of $\sigma_y = 280$ MPa, $n = 0.15$, $E = 70$ GPa, and $\nu = 0.3$ and by making use of the three representative indenter types. Each set of load and unload curves can be used to derive a pair of H_n/E_r and W_e/W.

Similar simulation processes were performed for various combinations of σ_y, n, V_r, and h_r. Figure 4 shows the plot of H_n/E_r versus W_e/W obtained for a purely flat-ended indenter with different bluntness levels. Each bluntness level is specified by a combination of V_r and h_r. Figures 5 and 6 show the results for purely conical-tipped and purely spherical-capped situations. Figure 7 shows the result for an ideal sharp indenter; i.e., $V_r = 1$, $h_r = 1$. One immediately sees that for a specific bluntness level, the data points of various n values delineate a functional relationship between H_n/E_r and W_e/W. Such a functional relationship can be expressed as a polynomial of W_e/W:

$$H_n/E_r = \sum_{i=1}^{6} [a_i(V_r, h_r)](W_e/W)^i \quad , \qquad (13)$$

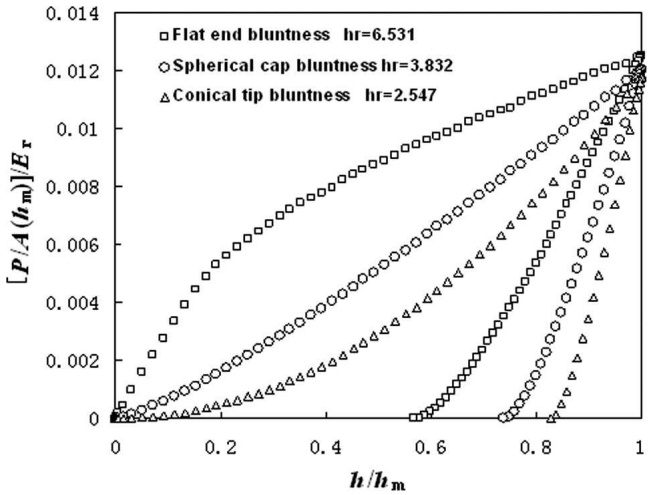

FIG. 3. Normalized load–displacement curves obtained from simulations at $\sigma_y = 280$ MPa, $n = 0.15$, $E = 70$ GPa, $\nu = 0.3$, and $V_r = 2.547$, with different h_r corresponding to the three representative blunt geometries.

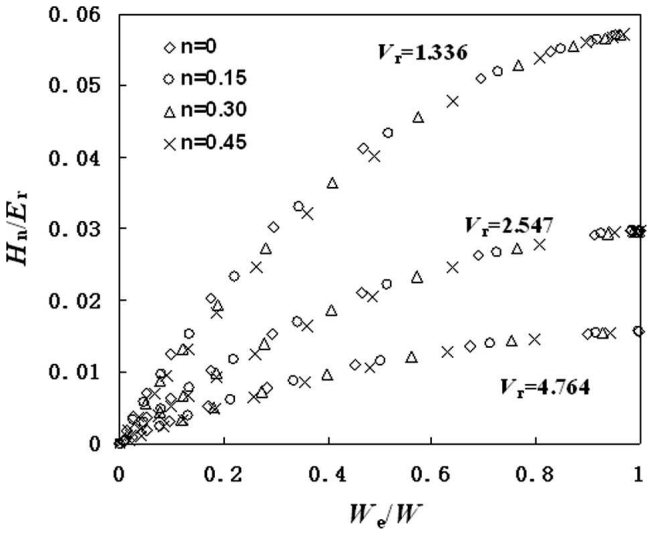

FIG. 5. Three H_n/E_r–W_e/W functional relationships for conical-tipped indenter with different bluntness levels specified with V_r and h_{rc} equal to 1.336, 2.547, 4.764 and 1.336, 2.547, 4.764, respectively, each containing data of n from 0 to 0.45.

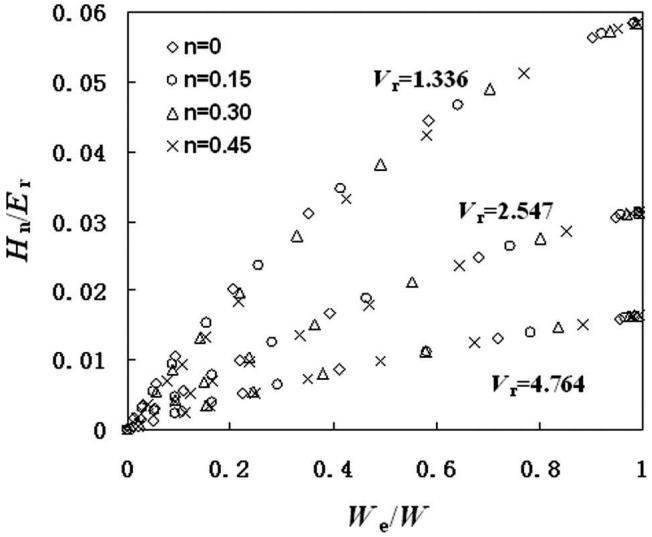

FIG. 4. Three H_n/E_r–W_e/W functional relationships for flat-ended indenter with different bluntness levels specified with V_r and h_{rf} equal to 1.336, 2.547, 4.764, and 2.712, 6.531, 13.240, respectively, each containing data of n from 0 to 0.45.

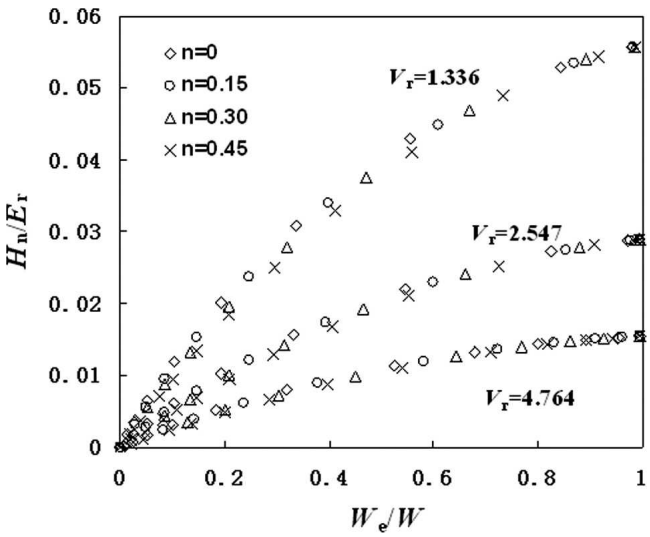

FIG. 6. Three H_n/E_r–W_e/W functional relationships for spherical-capped indenter with different bluntness levels specified with V_r and h_{rs} equal to 1.336, 2.547, 4.764 and 2.025, 3.832, 7.152, respectively, each containing data of n from 0 to 0.45.

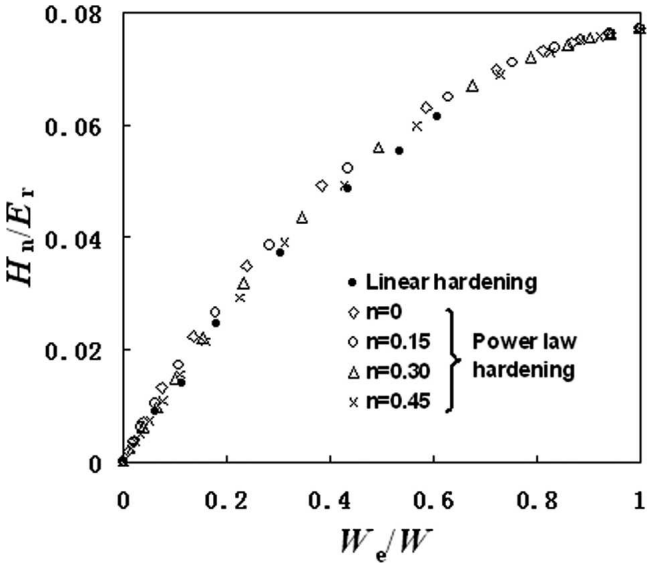

FIG. 7. Relationships between H_n/E_r and W_e/W for ideally sharp indenter based on power law hardening and linear work hardening with hardening modulus $E_l = 10\sigma_y$.

with $a_i(V_r, h_r)$ ($i = 1, \ldots, 6$) being the coefficients. Considering that V_r and h_r are not independent for a definite bluntness type, the relationships between H_n/E_r and W_e/W for the aforementioned three types of blunt tip geometries can be described, respectively, as:

$$(H_n/E_r)_{fj} = \sum_{i=1}^{6}[a_{fi}(V_{rj})](W_e/W)^i \quad , \qquad (14)$$

$$(H_n/E_r)_{cj} = \sum_{i=1}^{6}[a_{ci}(V_{rj})](W_e/W)^i \quad , \qquad (15)$$

$$(H_n/E_r)_{sj} = \sum_{i=1}^{6}[a_{si}(V_{rj})](W_e/W)^i \quad , \qquad (16)$$

where the subscripts f, c, and s refer to the flat-ended, conical-tipped, and spherical-capped bluntness, respectively. The values of the index $j = 1$, 2, 3, and 4 correspond to four selected bluntness levels described by volume bluntness ratios $V_{r1} = 1$, $V_{r2} = 1.336$, $V_{r3} = 2.547$, and $V_{r4} = 4.764$. Best fits to the numerical results as shown in Figs. 4 to 6 determine the coefficients $a_{fi}(V_{rj})$, $a_{ci}(V_{rj})$, and $a_{si}(V_{rj})$ for different V_{rj} values (Tables I to III). It should be pointed out that the H_n/E_r–W_e/W relationships for the spherical-capped geometry as well as the ideal one obtained in this analysis are slightly different from those obtained in our previous work.[15] The present results of H_n/E_r for definite W_e/W are slightly smaller than those of Ref. 15 because a larger overall dimension of the model is used in the present analysis. Results of this sensitivity test prove that the present setting can further improve the quality of the simulated results.

Also shown in Fig. 7 are data points of H_n/E_r against W_e/W obtained from Bolshakov and Pharr's results (denoted by "•") presented in Figs. 4, 7, 8, and 11 of Ref. 21 based on a linear hardening model with a hardening modulus $E_l = 10\ \sigma_y$. It is clearly shown that these H_n/E_r and W_e/W values obey a relationship similar to that derived from a Hollomon's hardening model, indicating that the method introduced in the present study is almost independent of the hardening model employed.

Figure 8 shows the best fits to the data shown in Figs. 4 to 6 by applying the function forms given by Eqs. (14) to (16). These fitting curves are used to express the functional relationships between H_n/E_r and W_e/W for the three typical indenter types. One immediately learns that for the same V_r, the change in h_r can also affect the trend of the function.

If a spherical-capped indenter model is used to derive the H_n/E_r value according to the experimental data produced by a real indenter having a tip shape inconsistent with the spherical-capped bluntness, the result could be misestimated by a certain amount. The range of misestimate of H_n/E_r for two extreme cases, i.e., flat-ended bluntness and conical-tipped bluntness, is reasonably evaluated by calculating the quantities $\delta_{fsj} \equiv [(H_n/E_r)_{sj} - (H_n/E_r)_{fj}]/(H_n/E_r)_{sj}$ and $\delta_{csj} \equiv [(H_n/E_r)_{sj} - (H_n/E_r)_{cj}]/(H_n/E_r)_{sj}$ for $j = 2$, 3, 4. From the results of δ_{fsj} and δ_{csj} as shown in Fig. 9, it can be seen that the maximum misestimate of H_n/E_r would lie between –9.9% and 12.5%. Further interpolation analysis based on the correlations of $(H_n/E_r)_{fj}$–W_e/W, $(H_n/E_r)_{cj}$–W_e/W, and $(H_n/E_r)_{sj}$–W_e/W ($j = 1$, 2, 3, 4) showed that even though the value of V_r is as small as 1.02, the misestimate of H_n/E_r based on the spherical-capped indenter model was still confined within the range between –1.0% and 0.4%, reflecting that the introduction of a parameter h_r is necessary for describing more correctly the real tip shape and degree of bluntness to produce a correct H_n/E_r–W_e/W relationship.

TABLE I. The values of coefficients $a_{fi}(V_{rj})$.

j	V_{rj}	$a_{f1}(V_{rj})$	$a_{f2}(V_{rj})$	$a_{f3}(V_{rj})$	$a_{f4}(V_{rj})$	$a_{f5}(V_{rj})$	$a_{f6}(V_{rj})$
1	1.000	0.16716	–0.13875	0.06215	0.01568	-0.04784	0.01878
2	1.336	0.11088	–0.13538	0.30236	–0.50340	0.41954	–0.13528
3	2.547	0.05344	–0.07060	0.18858	–0.31453	0.25048	–0.07588
4	4.764	0.02776	–0.03934	0.10015	–0.15016	0.10604	–0.02790

$i = 1, \ldots, 6$; $j = 1, \ldots, 4$ for different V_{rj}.

TABLE II. The values of coefficients $a_{ci}(V_{rj})$.

j	V_{rj}	$a_{c1}(V_{rj})$	$a_{c2}(V_{rj})$	$a_{c3}(V_{rj})$	$a_{c4}(V_{rj})$	$a_{c5}(V_{rj})$	$a_{c6}(V_{rj})$
1	1.000	0.16716	−0.13875	0.06215	0.01568	−0.04784	0.01878
2	1.336	0.12655	−0.14012	0.20772	−0.29096	0.22433	−0.07001
3	2.547	0.06482	−0.07744	0.14161	−0.22246	0.18104	−0.05782
4	4.764	0.03393	−0.04164	0.08170	−0.13158	0.10712	−0.03376

$i = 1, \ldots, 6$; $j = 1, \ldots, 4$ for different V_{rj}.

TABLE III. The values of coefficients $a_{si}(V_{rj})$.

j	V_{rj}	$a_{s1}(V_{rj})$	$a_{s2}(V_{rj})$	$a_{s3}(V_{rj})$	$a_{s4}(V_{rj})$	$a_{s5}(V_{rj})$	$a_{s6}(V_{rj})$
1	1.000	0.16716	−0.13875	0.06215	0.01568	−0.04784	0.01878
2	1.336	0.11612	−0.14391	0.29892	−0.50592	0.43731	−0.14669
3	2.547	0.05899	−0.06815	0.13162	−0.21203	0.17552	−0.05691
4	4.764	0.03104	−0.03438	0.06404	−0.10089	0.08154	−0.02588

$i = 1, \ldots, 6$; $j = 1, \ldots, 4$ for different V_{rj}.

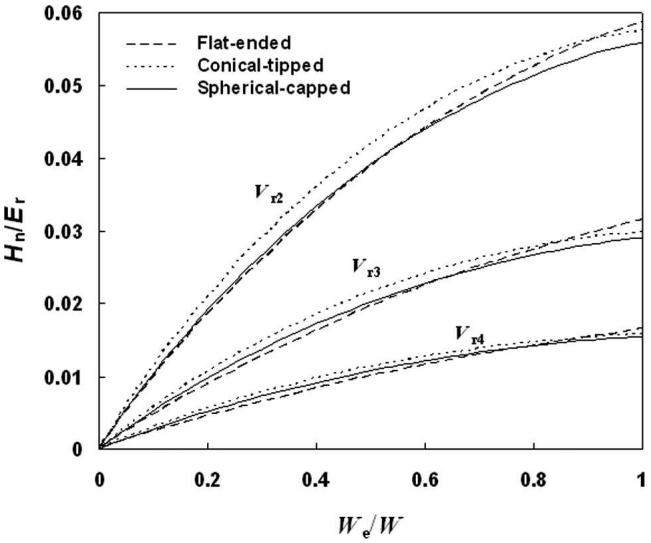

FIG. 8. Functional relationships $(H_n/E_r)_{fj}$–W_e/W (dashed line), $(H_n/E_r)_{cj}$–W_e/W (dotted line), and $(H_n/E_r)_{sj}$–W_e/W (solid line) for three typical indenter types produced by the best fits to the data in Figs. 4 to 6 with the use of expressions (14) to (16).

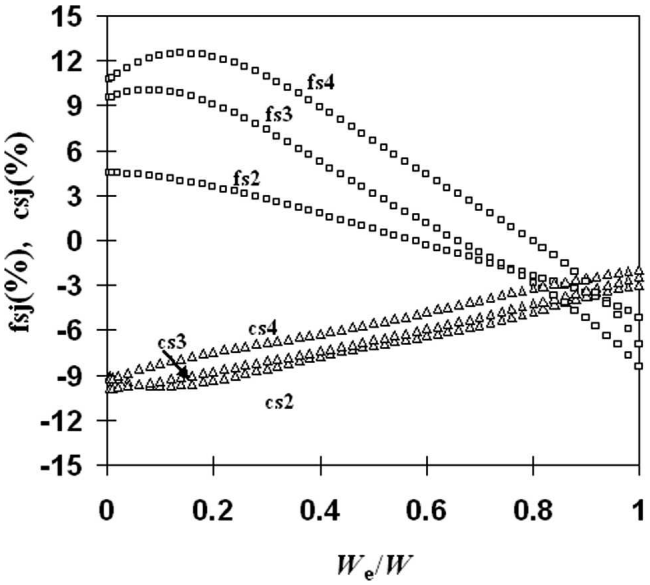

FIG. 9. δ_{fsj} and δ_{csj} versus W_e/W for three degrees of bluntness labeled by $j = 2$, 3, and 4.

In addition, the interpolation analysis showed that when the value of V_r is smaller than 1.006, the value of H_n/E_r estimated for a blunt indenter will be smaller than that for an ideal indenter by no more than 1.0%.

IV. METHOD FOR DETERMINING YOUNG'S MODULUS

Based on the polynomials (14) to (16) with the coefficients tabulated in Tables I to III, an improved method for determining Young's modulus is developed that is applicable to any real Berkovich indenter tip with an arbitrary tip shape and degree of bluntness. Detailed procedures of analysis are:

(i) Calibrate the area function $A(h)$ of a real Berkovich indenter used for indentation tests according to the tip calibration procedures proposed by Oliver and Pharr.[4,6]

(ii) Generate loading and unloading curves by performing indentations on the tested material with a depth-sensing indentation system. P_m and h_m are directly measured, and $A(h_m)$ is derived from the tip-calibration function. Hence, the value of the nominal hardness $H_n \equiv P_m/A(h_m)$ is determined. Further, the work ratio W_e/W is determined, where W_e and W are obtained by integrating the areas under the unloading and loading curves, respectively.

(iii) Calculate the volume bluntness ratio $V_r \equiv V_{ideal}/V_{blunt}$, where $V_{ideal} = (1/3)A(h_m)[A(h_m)/24.5]^{0.5}$ for an ideal Berkovich indenter, and $V_{blunt} = \int_0^{h_m} A(h)dh$ for the real Berkovich indenter.

(iv) Calculate the height bluntness ratio $h_r \equiv h_{ideal}/h_m$ for the real Berkovich indenter, where $h_{ideal} = [A(h_m)/24.5]^{0.5}$. Then, calculate the height bluntness ratios h_{rf}, h_{rc}, and h_{rs} associated with the three typical types of blunt tips by substituting the V_r value obtained in (iii) into the expressions relating the two bluntness ratios given in Sec. II.

(v) Write down the expressions (14) to (16) with the coefficients tabulated in Tables I to III for the three typical tip shapes and four different levels of bluntness specified by assigning V_{rj} with the values of 1, 1.336, 2.547, and 4.764 corresponding to $j = 1, \ldots, 4$. Then substitute W_e/W into the formulas to calculate the values of $(H_n/E_r)_{fj}$, $(H_n/E_r)_{cj}$, and $(H_n/E_r)_{sj}$, with $j = 1, 2, 3, 4$ corresponding to three typical tip shapes and four different bluntness levels.

(vi) Derive the best fit to the four data points of $(H_n/E_r)_{fj}$ versus V_{rj} ($j = 1, 2, 3, 4$) by using a third-order polynomial of $1/V_{rj}$. A best estimate of $(H_n/E_r)_f$ corresponding to V_r is thus derived via interpolation. The best estimates of $(H_n/E_r)_c$ and $(H_n/E_r)_s$ are obtained with the same technique.

(vii) Derive the best fit to the data points of $(H_n/E_r)_f$, $(H_n/E_r)_c$, and $(H_n/E_r)_s$ obtained in (iv) versus respectively values of h_{rf}, h_{rc}, and h_{rs} by using a second-order polynomial of h_r. Based on this relationship, a best estimate of H_n/E_r at V_r and h_r is derived by interpolation.

(viii) Determine $E_r = H_n/(H_n/E_r)$, and then E of the tested material by using the expression $E = (1 - \nu^2)/[1/E_r - (1 - \nu_i^2)/E_i]$, provided that the values of E_i, ν_i, and ν are all known.

V. EXPERIMENTAL EXAMPLES

In this section, we present the results obtained by applying the proposed method. Two materials, i.e., S45C carbon steel and 6061 aluminum alloy, were selected for investigation. Two specimens of the materials were polished to produce mirror-reflecting surfaces for indentation tests. The polishing processes were performed using grinding papers of 800, 1200, 2000, and 4000 grits, and then diamond pastes of 6, 3, 1, and 0.25 μm grain sizes. Atomic force microscopy analysis showed that the root mean square roughness of the polished surface was around 0.5 nm in a detected surface of 15 μm^2. To obtain references of the E values, uniaxial tensile tests for the two selected materials were performed. Results for the S45C carbon steel and 6061 aluminum alloy are found to be 200.1 and 70.5 GPa, respectively. Detailed rationale for using the results obtained from this test as references of E is given in our previous paper.[15]

A commercial Nano Indenter XP (MTS Systems Corp., Knoxville, TN) equipped with a Berkovich indenter was used for the measurements. The area function $A(h)$ of the indenter was derived according to Oliver and Pharr's procedures.[4,6] Indentation tests with full loads of 0.315 and 0.312 mN were performed on a carbon steel specimen and a 6061 aluminum alloy specimen. Each indentation test consisted of an approaching segment, a loading segment, a holding segment, an unloading segment, and a thermal drift correction segment. Five repetitive measurements were conducted at different positions on a sample surface to give an average result. Typical load–unload curves for S45C carbon steel and 6061 aluminum alloy are shown in Figs. 10 and 11. Influences caused by thermal drift and load frame stiffness were diminished through standard correction procedures. We take the experimental curve shown in Fig. 10 as an example to demonstrate the program of determining E, and the main results of different analysis steps described in

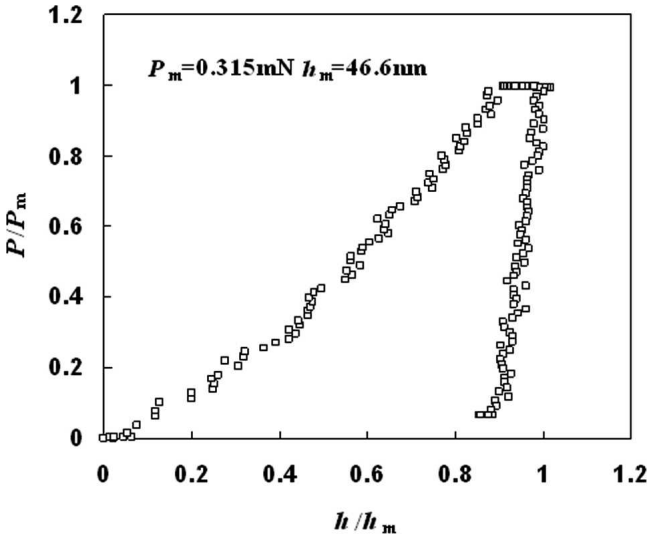

FIG. 10. Typical nanoindentation load-displacement curves for S45C carbon steel.

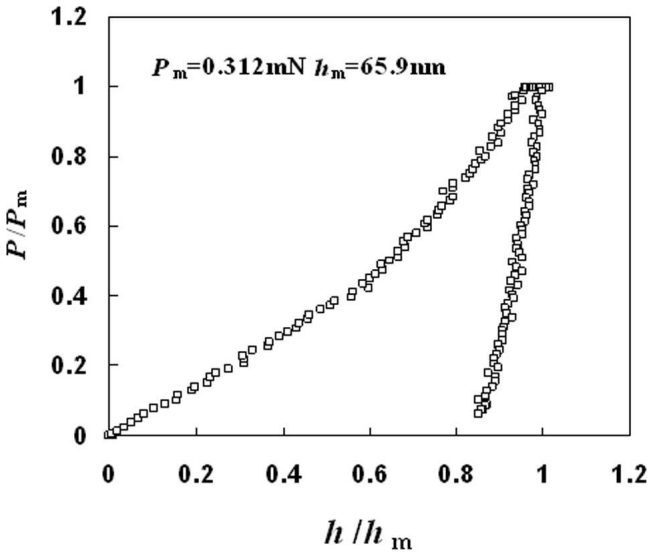

FIG. 11. Typical nanoindentation load-displacement curves for 6061 aluminum alloy.

TABLE IV. The main results of respective analysis steps as described in Sec. IV for Test 1 on S45C carbon steel.

Steps	Main results
(i)	$A(h) = 26.2644h^2 + 1255.2840h - 1951.4068h^{1/2} - 61.7471h^{1/4} + 945.9002h^{1/8}$
(ii)	$P_m = 0.315$ mN, $h_m = 46.6$ nm, $H_n \equiv P_m/A(h_m) = 3.02$GPa, $W_e/W = 0.126$
(iii)	$V_r \equiv V_{ideal}/V_{blunt} = (1/3)A(h_m)[A(h_m)/24.5]^{0.5}/\int_0^{h_m} A(h)dh = 1.186$
(iv)	$h_r \equiv h_{ideal}/h_m = [A(h_m)/24.5]^{0.5}/h_m = 1.395$, $h_{rf} = 1/[1-(1-1/V_r)^{1/3}] = 2.172$, $h_{rc} = V_r = 1.186$, $h_{rs} = 1/\{1-[(1-1/V_r)/(1+\sin\theta)]^{1/3}\}$ 1.762
(v)	$(H_n/E_r)_{fj} = \sum_{i=1}^{6}[a_{fi}(V_{rj})](W_e/W)^i = 0.0190, 0.0123, 0.0059, 0.0030$ for $j = 1, 2, 3, 4$
	$(H_n/E_r)_{cj} = \sum_{i=1}^{6}[a_{ci}(V_{rj})](W_e/W)^i = 0.0190, 0.0141, 0.0072, 0.0037$ for $j = 1, 2, 3, 4$
	$(H_n/E_r)_{sj} = \sum_{i=1}^{6}[a_{si}(V_{rj})](W_e/W)^i = 0.0190, 0.0128, 0.0066, 0.0035$ for $j = 1, 2, 3, 4$
(vi)	$(H_n/E_r)_f = \sum_{k=1}^{4}[(H_n/E_r)_{fk}\prod_{\substack{j=1\\j\neq 1}}^{4}(1/V_r - 1/V_{rj})/(1/V_{rk} - 1/V_{rj})] = 0.0145$
	$(H_n/E_r)_c = \sum_{k=1}^{4}[(H_n/E_r)_{ck}\prod_{\substack{j=1\\j\neq 1}}^{4}(1/V_r - 1/V_{rj})/(1/V_{rk} - 1/V_{rj})] = 0.0159$
	$(H_n/E_r)_s = \sum_{k=1}^{4}[(H_n/E_r)_{sk}\prod_{\substack{j=1\\j\neq 1}}^{4}(1/V_r - 1/V_{rj})/(1/V_{rk} - 1/V_{rj})] = 0.0149$
(vii)	$H_n/E_r = (H_n/E_r)_f\{(h_r - h_{rc})(h_r - h_{rs})/[(h_{rf} - h_{rc})(h_{rf} - h_{rs})]\} + (H_n/E_r)_c\{(h_r - h_{rf})(h_r - h_{rs})/[h_{rc} - h_{rf})(h_{rc} - h_{rs})]\}$ $+ (H_n/E_r)_s\{(h_r - h_{rf})(h_r - h_{rc})/[(h_{rs} - h_{rf})(h_{rs} - h_{rc})]\} = 0.0155$
(viii)	$E_r = H_n/(H_n/E_r) = 196.5$ GPa, $E = (1-\nu^2)/[1/E_r - (1-\nu_i^2)/E_i] = 215.8$ GPa

Sec. IV are listed in Table IV. For comparison, we applied our previous method based on a single-parameter spherical-capped indenter model to deduce the results, which were found to be $E_{rs} = H_n/(H_n/E_r)_s = 204.2$ GPa and $E_s = (1-\nu^2)/[1/E_{rs} - (1-\nu_i^2)/E_i] = 226.1$GPa (subscript "s" refers to the spherical-capped model). A noticeable difference between E and E_s is observed.

Analyses of repetitive tests on S45C carbon steel and 6061 aluminum alloy were performed with the same procedures. Results obtained are shown in Table V. It can be seen that the average values determined from the current method for the two materials are smaller and closer to the reference values than those from the previous method. This improvement is attributed to the use of a more reasonable model of tip geometry. This is understood as according to the fact that the value of height bluntness ratio $h_{rc} < h_r < h_{rs}$, the indenter used in the experiments should have a shape between a typical conical-tipped shape and a spherical-capped shape. Figure 12 shows the equivalent radial profile of the real indenter tip used in our nanoindentation tests. Also shown in the figure are the profiles of an ideal tip and the three representative indenter models, i.e., conical-tipped, flat-ended, and spherical-capped bluntness. It shows clearly that the shape of the real indenter tip is closer to a conical-tipped geometry. Thus the value of $(H_n/E_r)_s$ should always be smaller than the value of H_n/E_r. This is clearly demonstrated in Fig. 8. As such, the values of E_s deduced from $E_s = H_n/(H_n/E_r)_s$ would always be larger than the values of E calculated from $E = H_n/(H_n/E_r)$. In addition, the results of Young's modulus $E_{O\&P}$ determined by the Oliver and Pharr method are also shown in Table V. It is obvious that for a material such as S45C carbon steel with a moderate strain-hardening exponent of about 0.15, the traditional method may provide a good estimate on the Young's modulus, while for a material such as 6061 aluminum alloy with a small strain-hardening exponent of about 0.04, the currently proposed method appears to be more effective than the traditional one. It is thus further believed that the relatively low strain-hardening exponent of 6061 aluminum alloy would cause a pileup effect, which is supposed to be the main reason responsible for the lower accuracy in estimating the Young's modulus of the material using the Oliver and Pharr method.

Finally, we point out that to date there is no effective method to correlate the indentation data and the elastic moduli of an elastoplastically anisotropic solid because of the complexity of the problem itself. However, one can still gain an insight into the meaning of the nominal Young's modulus of an elastically anisotropic material obtained from indentation, which is denoted as indentation modulus thereafter. According to the analysis of Vlassak et al.,[22–24] the indentation modulus of an

TABLE V. The values of E, E_s, and $E_{O\&P}$ for S45C carbon steel and 6061 aluminum alloy determined from the current method, the model based on the spherical-capped geometry and Oliver and Pharr method.

	For S45C carbon steel														
Test no.	h_m (nm)	h_r	V_r	W_e/W	H_n (GPa)	$(H_n/E_r)_f$	$(H_n/E_r)_c$	$(H_n/E_r)_s$	H_n/E_r	E (GPa)	E_s (GPa)	$E_{O\&P}$ (GPa)	$(E-200.1)/E$	$(E_s-200.1)/E_s$	$(E_{O\&P}-200.1)/E_{O\&P}$
1	46.6	1.395	1.186	0.126	3.041	0.0145	0.0159	0.0149	0.0155	215.8	226.1	197.6	7.3%	11.5%	−1.3%
2	45.7	1.401	1.190	0.128	3.138	0.0147	0.0161	0.0150	0.0156	221.3	232.0	211.2	9.6%	13.8%	5.3%
3	45.2	1.404	1.192	0.129	3.193	0.0147	0.0162	0.0151	0.0157	224.7	235.8	202.7	10.9%	15.1%	1.3%
4	40.6	1.435	1.212	0.170	3.787	0.0184	0.0202	0.0188	0.0196	211.3	221.8	206.1	5.3%	9.8%	2.9%
5	43.5	1.415	1.199	0.128	3.395	0.0145	0.0160	0.0149	0.0155	246.3	258.8	256.9	18.8%	22.7%	22.1%
Average	44.3	1.410	1.196	0.136	3.311	0.0154	0.0169	0.0157	0.0164	223.9	234.9	214.9	10.4%	14.6%	6.9%
Std. dev.	2.4	0.016	0.010	0.019	0.296	0.0017	0.0019	0.0017	0.0018	13.5	14.4	24.0			

	For 6061 aluminum alloy														
Test no.	h_m (nm)	h_r	V_r	W_e/W	H_n (GPa)	$(H_n/E_r)_f$	$(H_n/E_r)_c$	$(H_n/E_r)_s$	H_n/E_r	E (GPa)	E_s (GPa)	$E_{O\&P}$ (GPa)	$(E-70.5)/E$	$(E_s-70.5)/E_s$	$(E_{O\&P}-70.5)/E_{O\&P}$
1	64.6	1.314	1.138	0.191	1.768	0.0223	0.0239	0.0226	0.0234	72.2	74.7	76.3	2.4%	5.6%	7.6%
2	60.1	1.330	1.147	0.223	1.992	0.0251	0.0269	0.0255	0.0263	72.2	74.7	77.4	2.4%	5.6%	8.9%
3	64.8	1.313	1.137	0.202	1.759	0.0234	0.0250	0.0237	0.0245	68.3	70.6	80.5	−3.2%	0.1%	12.4%
4	62.1	1.323	1.143	0.184	1.888	0.0214	0.0230	0.0218	0.0225	80.6	83.5	91.4	12.5%	15.6%	22.9%
5	65.9	1.309	1.135	0.164	1.711	0.0196	0.0210	0.0199	0.0206	79.9	82.7	93.1	11.8%	14.8%	24.3%
Average	63.5	1.318	1.140	0.193	1.824	0.0224	0.0240	0.0227	0.0235	74.6	77.2	83.7	5.2%	8.3%	15.8%
Std. dev.	2.4	0.009	0.005	0.022	0.115	0.0021	0.0022	0.0021	0.0021	5.4	5.6	7.9			

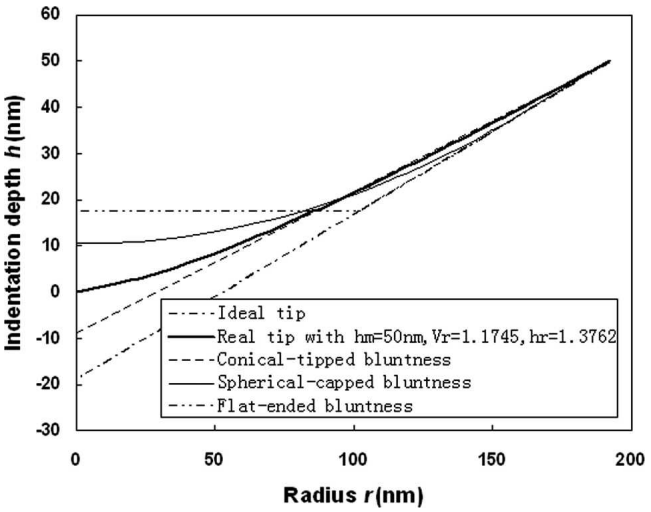

FIG. 12. Equivalent radial profiles of the real indenter tip used in the present study (h_m = 50 nm, V_r = 1.1745, and h_r = 1.3762), an ideal tip and the three representative indenter models (conical-tipped, flat-ended, and spherical-capped bluntness).

anisotropic material behaves differently from the real elastic modulus associated with the crystallographic direction along which the load is applied. The difference between the indentation moduli for different crystallographic directions is always much smaller than that between two elastic moduli associated with the respective crystallographic directions. The influence of anisotropy on the indentation modulus is substantially diminished by the loading mode of indentation. In fact, intruding an indenter into a crystal causes multiaxial stresses, so the indentation modulus thus obtained should represent some average of elastic moduli of different crystallographic directions. It has been shown that for most of the cubic crystals having an anisotropy ratio less than 3 to ~4, such as Al, Ag, Au, Cr, Cu, Fe, Ge, Mo, Nb, Ni, Pb, Ta, Si, V, W, TiC, diamond, MgO, etc.,[25] the indentation modulus values corresponding to different crystallographic directions would not deviate from its polycrystalline indentation modulus by more than 12%. Therefore, the indentation modulus measured by a nanoindentation test can be regarded as a good estimate of the polycrystalline modulus for a material with small or moderate anisotropy. As for a material with larger anisotropy such as zinc single crystal, it is difficult to determine the polycrystalline indentation modulus by indentation test in only one direction.

VI. CONCLUSIONS

A volume bluntness ratio V_r and a height bluntness ratio h_r were introduced to describe the blunt tip geometry of a real Berkovich indenter. The volume bluntness ratio is defined as $V_r \equiv V_{ideal}/V_{blunt}$. V_{ideal} is the part of the volume of an ideal Berkovich indenter bounded by the cross-sectional area $A(h_m)$, namely the cross-sectional area of the real indenter measured at the maximum displacement h_m. V_{blunt} is the part of the volume of the real indenter bounded by the same area $A(h_m)$. The height bluntness ratio is defined as $h_r \equiv h_{ideal}/h_m$, in which h_{ideal} is the indentation depth of the ideal indenter calculated from the ideal tip point to the cross-sectional area with a

magnitude $A(h_m)$. Dimensional analysis and finite element method are employed to investigate the indentation responses. Three representative nonideal indenter geometries, i.e., flat-ended geometry, conical-tipped geometry with a half-included conical angel α larger than $\theta = 70.3°$, and spherical-capped geometry with bluntness specified by V_r and h_r are used for analysis. It is shown that for a set of definite values of V_r and h_r, a functional relationship between H_n/E_r and W_e/W for each of the three selected indenter geometries can be found. In particular, the results of H_n/E_r derived from a model based on a spherical-capped geometry could have a misestimate as large as −9.9% to 12.5%, if the shape of the real indenter tip deviates significantly from a typical spherical-capped geometry and has an extremely large bluntness. Based on the H_n/E_r–W_e/W relationships associated with different indenter shapes and degrees of bluntness specified by a certain set of V_r and h_r, an improved energy-based method for determining Young's modulus with an arbitrarily blunt Berkovich indenter was developed. The procedures of analysis were established. The superiority of the method was demonstrated by applying it to S45C carbon steel and 6061 aluminum alloy.

ACKNOWLEDGMENT

This work was supported by the National Natural Science Foundation of China (Grant Nos. 10672185, 10432050, and 10572142).

REFERENCES

1. J.B. Pethica, R. Hutchings, and W.C. Oliver: Hardness measurement at penetration depth as small as 20 nm. *Philos. Mag. A* **48,** 593 (1983).
2. J.L. Loubet, J.M. Georges, O. Marchesini, and G. Meille: Vickers indentation curves of magnesium oxide (MgO). *J. Tribol.* **106,** 43 (1984).
3. D. Newey, M.A. Wilkens, and H.M. Pollock: An ultra-low-load penetration hardness tester. *J. Phys. E.: Sci. Instrum.* **15,** 119 (1982).
4. W.C. Oliver and G.M. Pharr: An improved technique for determining hardness and elastic modulus using load and displacement sensing indentation experiments. *J. Mater. Res.* **7,** 1564 (1992).
5. G.M. Pharr, W.C. Oliver, and F.R. Brotzen: On the generality of the relationship among contact stiffness, contact area, and elastic modulus during indentation. *J. Mater. Res.* **7,** 613 (1992).
6. W.C. Oliver and G.M. Pharr: Measurement of hardness and elastic modulus by instrumented indentation: Advances in understanding and refinements to methodology. *J. Mater. Res.* **19,** 3 (2004).
7. Y-T. Cheng and C.M. Cheng: Scaling, dimension analysis, and indentation measurements. *Mater. Sci. Eng., R* **44,** 91 (2004).
8. A.C. Fischer-Cripps: *Nanoindentation* (Springer-Verlag, New York, 2004), p. 39.
9. J. Malzbender and G. de With: Indentation load-displacement curve, plastic deformation, and energy. *J. Mater. Res.* **17,** 502 (2002).
10. T.A. Venkatesh, K.J. Van Vliet, A.E. Giannakopoulos, and S. Suresh: Determination of elasto-plastic properties by instrumented sharp indentation: Guidelines for property extraction. *Scr. Mater.* **42,** 833 (2000).
11. A.E. Giannakopoulos and S. Suresh: Determination of elasto-plastic properties by instrumented sharp indentation. *Scr. Mater.* **40,** 1191 (1999).
12. Y-T. Cheng and C-M. Cheng: Relationships between hardness, elastic modulus, and the work of indentation. *Appl. Phys. Lett.* **73,** 614 (1998).
13. C-M. Cheng and Y-T. Cheng: On the initial unloading slope in indentation of elastic-plastic solids by an indenter with an axisymmetric smooth profile. *Appl. Phys. Lett.* **71,** 2623 (1997).
14. W.Y. Ni, Y.T. Cheng, C.M. Chen, and D.S. Grummon: An energy-based method for analyzing instrumented spherical indentation experiments. *J. Mater. Res.* **19,** 149 (2004).
15. D. Ma, C.W. Ong, S.F. Wong, and J. He: New method for determining Young's modulus by non-ideally sharp indentation. *J. Mater. Res.* **20,** 1498 (2005).
16. D. Ma, C.W. Ong, and S.F. Wong: New relationship between Young's modulus and nonideally sharp indentation parameters. *J. Mater. Res.* **19,** 2144 (2004).
17. M. Dao, N. Chollacoop, K.J. Van Vliet, T.A. Venkatesh, and S. Suresh: Computational modeling of the forward and reverse problems in instrumented sharp indentation. *Acta Mater.* **49,** 3899 (2001).
18. M. Lichinchi, C. Lenardi, J. Haupt, and R. Vitali: Simulation of Berkovich nanoindentation experiments on thin films using finite element method. *Thin Solid Films* **312,** 240 (1998).
19. A.C. Fischer-Cripps: Use of combined elastic modulus in depth-sensing indentation with a conical indenter. *J. Mater. Res.* **18,** 1043 (2003).
20. ABAQUS: Version 6.2 (Hibbitt, Karlsson & Sorensen, Inc., Pawtucket, RI, 2001).
21. A. Bolshakov and G.M. Pharr: Influences of pileup on the measurement of mechanical properties by load and depth sensing indentation techniques. *J. Mater. Res.* **13,** 1049 (1998).
22. J.J. Vlassak and W.D. Nix: Measuring the elastic properties of anisotropic materials by means of indentation experiments. *J. Mech. Phys. Solids* **42,** 1223 (1994).
23. J.J. Vlassak and W.D. Nix: Indentation modulus of elastically anisotropic half spaces. *J. Mech. Phys. Solids* **67,** 1045 (1993).
24. J.J. Vlassak, M. Ciavarella, J.R. Barber, and X. Wang: The indentation modulus of elastically anisotropic materials for indenters of arbitrary shape. *J. Mech. Phys. Solids* **51,** 1701 (2003).
25. J.P. Hirth and J. Lothe: Elastic Constants, in *Theory of Dislocations* (Krieger Publishing Company, Malabar, FL, 1982), p. 837.